

Growth of high material quality InAs/GaSb type-II superlattice for long-wavelength infrared range by molecular beam epitaxy

Fang-Qi Lin(林芳祁), Nong Li(李农), Wen-Guang Zhou(周文广), Jun-Kai Jiang(蒋俊锴), Fa-Ran Chang(常发冉), Yong Li(李勇), Su-Ning Cui(崔素宁), Wei-Qiang Chen(陈伟强), Dong-Wei Jiang(蒋洞微), Hong-Yue Hao(郝宏玥), Guo-Wei Wang(王国伟), Ying-Qiang Xu(徐应强), and Zhi-Chuan Niu(牛智川)

Citation: Chin. Phys. B, 2022, 31 (**9**): 098504. DOI: 10.1088/1674-1056/ac615d
Journal homepage: http://cpb.iphy.ac.cn; http://iopscience.iop.org/cpb

What follows is a list of articles you may be interested in

Wet etching and passivation of GaSb-based very long wavelength infrared detectors

Xue-Yue Xu(许雪月), Jun-Kai Jiang(蒋俊锴), Wei-Qiang Chen(陈伟强), Su-Ning Cui(崔素宁), Wen-Guang Zhou(周文广), Nong Li(李农), Fa-Ran Chang(常发冉), Guo-Wei Wang(王国伟), Ying-Qiang Xu(徐应强), Dong-Wei Jiang(蒋洞微), Dong-Hai Wu(吴东海), Hong-Yue Hao(郝宏玥), and Zhi-Chuan Niu(牛智川)

Chin. Phys. B, 2022, 31 (**6**): 068503. DOI: 10.1088/1674-1056/ac4cc1

Investigation of active-region doping on InAs/GaSb long wave infrared detectors

Su-Ning Cui(崔素宁), Dong-Wei Jiang(蒋洞微), Ju Sun(孙矩), Qing-Xuan Jia(贾庆轩), Nong Li(李农), Xuan Zhang(张璇), Yong Li(李勇), Fa-Ran Chang(常发冉), Guo-Wei Wang(王国伟), Ying-Qiang Xu(徐应强), Zhi-Chuan Niu(牛智川)

Chin. Phys. B, 2020, 29 (**4**): 048502. DOI: 10.1088/1674-1056/ab773c

High quantum efficiency long-/long-wave dual-color type-Ⅱ InAs/GaSb infrared detector

Zhi Jiang(蒋志), Yao-Yao Sun(孙姚耀), Chun-Yan Guo(郭春妍), Yue-Xi Lv(吕粤希), Hong-Yue Hao(郝宏玥), Dong-Wei Jiang(蒋洞微), Guo-Wei Wang(王国伟), Ying-Qiang Xu(徐应强), Zhi-Chuan Niu(牛智川)

Chin. Phys. B, 2019, 28 (**3**): 038504. DOI: 10.1088/1674-1056/28/3/038504

Performance of dual-band short- or mid-wavelength infrared photodetectors based on InGaAsSb bulk materials and InAs/GaSb superlattices

Yao-yao Sun(孙姚耀), Yue-xi Lv(吕粤希), Xi Han(韩玺), Chun-yan Guo(郭春妍), Zhi Jiang(蒋志), Hong-yue Hao(郝宏玥), Dong-wei Jiang(蒋洞微), Guo-wei Wang(王国伟), Ying-qiang Xu(徐应强), Zhi-chuan Niu(牛智川)

Chin. Phys. B, 2017, 26 (**9**): 098506. DOI: 10.1088/1674-1056/26/9/098506

Very long wavelength infrared focal plane arrays with 50% cutoff wavelength based on type-II InAs/GaSb superlattice

Xi Han(韩玺), Wei Xiang(向伟), Hong-Yue Hao(郝宏玥), Dong-Wei Jiang(蒋洞微), Yao-Yao Sun(孙姚耀), Guo-Wei Wang(王国伟), Ying-Qiang Xu(徐应强), Zhi-Chuan Niu(牛智川)

Chin. Phys. B, 2017, 26 (**1**): 018505. DOI: 10.1088/1674-1056/26/1/018505

Growth of high material quality InAs/GaSb type-II superlattice for long-wavelength infrared range by molecular beam epitaxy

Fang-Qi Lin(林芳祁)[1,2], Nong Li(李农)[1,2], Wen-Guang Zhou(周文广)[1,2], Jun-Kai Jiang(蒋俊锴)[1,2], Fa-Ran Chang(常发冉)[1], Yong Li(李勇)[1], Su-Ning Cui(崔素宁)[1,2], Wei-Qiang Chen(陈伟强)[1,2], Dong-Wei Jiang(蒋洞微)[1,2,3], Hong-Yue Hao(郝宏玥)[1,2,3], Guo-Wei Wang(王国伟)[1,2,3,†], Ying-Qiang Xu(徐应强)[1,2,3,‡], and Zhi-Chuan Niu(牛智川)[1,2,3,§]

[1] *State Key Laboratory for Superlattices and Microstructures, Institute of Semiconductors, Chinese Academy of Sciences, Beijing* 100083, *China*
[2] *College of Materials Science and Opto-Electronic Technology, University of Chinese Academy of Sciences, Beijing* 100049, *China*
[3] *Center of Materials Science and Optoelectronics Engineering, University of Chinese Academy of Sciences, Beijing* 100049, *China*

(Received 29 December 2021; revised manuscript received 3 March 2022; accepted manuscript online 28 March 2022)

By optimizing the V/III beam-equivalent pressure ratio, a high-quality InAs/GaSb type-II superlattice material for the long-wavelength infrared (LWIR) range is achieved by molecular beam epitaxy (MBE). High-resolution x-ray diffraction (HRXRD), atomic force microscopy (AFM), and Fourier transform infrared (FTIR) spectrometer are used to characterize the material growth quality. The results show that the full width at half maximum (FWHM) of the superlattice zero-order diffraction peak, the mismatching of the superlattice zero-order diffraction peak between the substrate diffraction peaks, and the surface roughness get the best results when the beam-equivalent pressure (BEP) ratio reaches the optimal value, which are 28 arcsec, 13 arcsec, and 1.63 Å, respectively. The intensity of the zero-order diffraction peak is strongest at the optimal value. The relative spectral response of the LWIR detector shows that it exhibits a 100% cut-off wavelength of 12.6 μm at 77 K. High-quality epitaxial materials have laid a good foundation for preparing high-performance LWIR detector.

Keywords: type-II superlattice, InAs/GaSb, long-wavelength, strain-balanced

PACS: 85.60.Gz, 68.65.Cd, 72.20.Jv **DOI:** 10.1088/1674-1056/ac615d

1. Introduction

Since G. A. Sai-Halasz, R. Tsu, and L. Esaki[1] firstly proposed the theory of type-II superlattices in 1977, after decades of theoretical scientific development and the progress of molecular beam epitaxy technology, it has aroused great interest from many researchers worldwide. In 1987, D. L. Smith and C. Mailhiot[2] proposed that type II superlattices could be used as excellent candidate materials for infrared detectors. The current state-of-the-art infrared detection technology is based on mercury cadmium telluride ($Hg_{1-x}Cd_xTe$) materials, and most commercial LWIR optical receivers are dominated by $Hg_{1-x}Cd_xTe$ material,[3,4] which can obtain high detectivity and fast response. $Hg_{1-x}Cd_xTe$ materials can be used for infrared detection based on PIN and avalanche photodiode (APD) structures.[5]

However, $Hg_{1-x}Cd_xTe$ has some defects, such as poor uniformity,[6] a high thermal expansion coefficient,[7] extreme sensitivity to component control,[8,9] and a large tunneling dark current[10–12] due to the low effective mass of electrons. The $Hg_xCd_{1-x}Te$ materials needed for infrared detectors are difficult to grow consistently on account of high sensitivity to alloy composition, which causes poor spatial uniformity. This problem is particularly severe in LWIR and very long-wavelength infrared detection (VLWIR). Other commercially available LWIR detectors[13] include Si:x,[14] vanadium oxide (V_xO_y),[15] and amorphous silicon (α-Si),[16] which have high operating temperatures (uncooled), good uniformity, compatibility with existing COMS processes, and low manufacturing costs. However, these photodetectors are limited by a narrow tunable wavelength range and poor detectivity.

Compared with other materials ($Hg_{1-x}Cd_xTe$, InSb, QWIP, QD, and V_xO_y, etc.), InAs/GaSb, as a typical type-II superlattice material, has many advantages,[17–19] such as accurate regulation of the band gap, high operating temperature,[20–22] large effective mass,[2] inhibition of Auger recombination,[23] broadband absorption, incident light at normal angle and good uniformity of material growth. The detection wavelength of InAs/GaSb type-II superlattice materials can be changed from near infrared to very long wave infrared only by adjusting the layer thickness of the InAs and GaSb layers.[24,25] Especially for long-wavelength infrared (LWIR)[26,27] and very long-wavelength infrared (VLWIR)[28–30] range detection, its advantage is obvious. Although InAs/GaSb T2SL was deemed a competitive candidate, the current efficiency is still far from expected. To further improve crystalline quality and device performance, many strategies, including optimizing the heterojunction interface by controlling the Sb/As background pressure and shutter sequence

†Corresponding author. E-mail: wangguowei@semi.c.cn
‡Corresponding author. E-mail: yingqxu@semi.ac.cn
§Corresponding author. E-mail: zcniu@semi.ac.cn

© 2022 Chinese Physical Society and IOP Publishing Ltd

during interface formation, using a migration-enhance epitaxy technique,[31,32] and introducing novel structures to suppress dark current,[33,34] have been adopted. These approaches have been proven to be very effective.

In this paper, we demonstrate that a high-quality strain-balanced InAs/GaSb type-II superlattice material for long-wavelength infrared range detection could be obtained by optimizing the V/III beam-equivalent pressure (BEP) ratio during the molecular beam epitaxy growth process. The long-wavelength InAs/GaSb superlattice materials prepared in various V/III BEP ratios were assessed by using high-resolution x-ray diffraction, atomic force microscopy and the relative spectral response.

2. Experiment

In our experiment, all epitaxial samples were grown on tellurium-doped n-type epi-ready GaSb (001) substrates by a Veeco Gen 20 molecular beam epitaxy system, which was equipped with group-III (Ga, In, and Al) SUMO dual-source cells and group-V (Sb_2 and As_2) valve crack sources. The detailed structure of the LWIR detector is shown in Fig. S4 of the supporting information. Before the growth of functional layers, the wafers were heated to 420 °C in a preparation module for 2 hours of degas and then heated to 680 °C in a growth module for 30 minutes to remove the surface oxide layers. After that, a thin GaSb buffer layer was deposited at 630 °C to keep the surface smooth. *In situ* reflection high-energy electron diffraction (RHEED) was used to monitor the substrate surface temperature and growth status. When the substrate surface temperature reached a typical temperature (marked as T_c), the electron diffraction pattern changed from 2×5 to 1×3, and T_c was defined as the transition temperature at which GaSb surface reconstruction ($2\times5 \leftrightarrow 1\times3$).[35] occurred at a given antimony flux. All these samples were grown at $T_c - 15$ °C.

During the serials growth of these samples, the As/In beam-equivalent pressure ratios were set at 2, 3, 4, 5, and 7, and the Sb/Ga BEP flux ratio was kept at 7. Then the Sb/Ga beam-equivalent pressure ratios were set at 5, 6, 7, 8, 9, and 10 (marked as A, B, C, D, E, and F), while the As/In beam-equivalent pressure ratio was kept at 3, and the more parameters detail are shown in Table 1 of supporting information. After the optimization of the 12.5 ML/8 ML InAs/GaSb superlattice absorption region, LWIR detectors were fabricated, as shown in Fig. S6. The device consisted of 7 functional layers from bottom to top: tellurium-doped n-type GaSb (001) substrates, GaSb buffer layer, bottom n-type contact layer and barrier sharing the same structure, which was composed of 18/3/5/3 MLS of InAs/GaSb/AlSb/GaSb superlattices. The p-type absorption regions share the same structure as the top p-type contact layer, which consists of 12.5/8 MLs of InAs/GaSb superlattices. Finally, a 200 nm GaSb layer cap was deposited to protect the superlattices.

After epitaxial growth of the functional layers, for all the samples, optical microscopy was used to observe and estimate surface defects by using a Nikon Eclipse LV100D optical microscope. The structural quality was assessed by symmetric (004) x-ray scans with a Bruker JV QC-3 high-resolution double-crystal x-ray diffractometer (HRXRD), and the surface morphology was studied by using a Park System NX20 atomic force microscope (AFM). The optical performance of the epitaxial layers was measured by using a Bruker Vertex-80 Fourier transform infrared (FTIR) spectrometer.

3. Results and discussion

To balance the strain of 12.5 MLs/8 MLs InAs/GaSb with the GaSb substrate, the InSb interface was adopted in this experiment. In each growth period, the nominal interface type was varied by using the techniques of migration-enhanced epitaxy (MEE). The indium and antimony shutters were kept open for a few seconds to generate the InSb interface between the InAs and GaSb layers. The mechanical shutter sequences used during the growth period in this work are illustrated in Fig. 1. Specifically, the indium shutter was kept open before and after the growth of the InAs layer for 2.9 seconds and 2.7 seconds, respectively. At a high growth rate, it is easy to form an InSb island structure. To improve the growth of the InSb interface, it was deposited by employing a low growth rate indium source. Similarly, the Sb shutter was kept open before and after the growth of the GaSb layer for 6 seconds and 3 seconds, respectively.

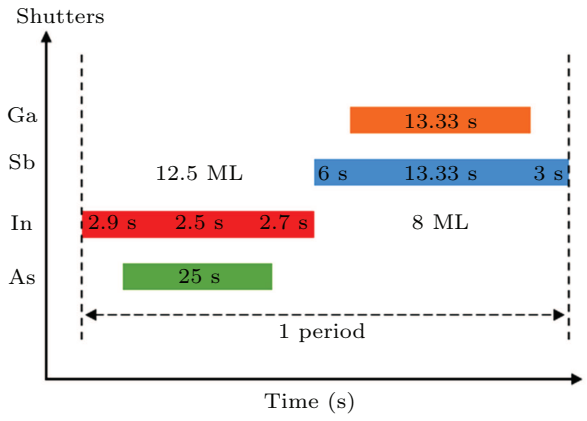


Fig. 1. The shutter sequence during per period.

From the high-resolution x-ray diffraction results shown in Figs. 2(a) and S1, in these samples, the Sb/Ga BEP flux ratio was kept at 7, and we can clearly see that lattice mismatch between the epitaxial layer and the substrate of the five samples falls first and then rises as the As/In BEP flux ratio rises. When the As/In BEP flux ratio is small, the tensile strain is not

exactly compensated, resulting in a compressive strain. When the As/In BEP flux is 3, the mismatch reaches a smallest value of 20 arcsec (165 ppm). When the As/In BEP flux ratio is large, the tensile stress becomes larger as the As/In BEP flux ratio rises. Similarly, from Figs. 2(b) and S3, we can see that lattice mismatch between the epitaxial layer and the substrate of the six samples falls first and then rises as the Sb/Ga BEP flux ratio rises. When the Sb/Ga BEP flux ratio is small, the InSb faces produced between the InAs layers and GaSb layers are not enough to balance the intrinsic tensile strain. When the Sb/Ga BEP flux is 8, the mismatch of sample D reaches a smallest value of 13 arcsec (108 ppm), but it produces too many InSb faces when the Sb/Ga BEP flux ratio is large, and the compressive stress becomes larger as the Sb/Ga BEP flux ratio rises.

The surface morphology roughness was evaluated by AFM, as shown in Figs. 2(a), 2(c), S2, and S3. Generally, the growth rate of epitaxial layers is determined by the III group element BEP flux, while the V/III BEP flux ratio will influence the nucleation process and then play a crucial role in the material surface quality.

To some extent, the FWHM and intensity of the zero-order diffraction peak from high-resolution x-ray diffraction can indicate the epitaxial quality of the heterogeneous interface. As shown in Fig. 2(d), when the Sb/Ga BEP flux ratio is too small or large, the intensity of the zero-order diffraction peak decreases considerably and reaches a maximum value of 5.52×10^6 when the Sb/Ga BEP flux ratio is 8. In contrast, the FWHM obtains a small value with 28 arcsec at 8. It should be noted that the FWHM of these samples are relatively close, which means that the interface of the six samples is flat with the same shutter sequences.

From the AFM results, whether there is too large or too little As/In ratio, many rod-shaped islands are generated on the surface. From the theory of film formation, they are not suitable for atoms to migrate to a reasonable lattice position to form a smooth and flat surface. When the As/In BEP and Sb/Ga flux is 3 and 7 respectively, the AFM images show an RMS surface roughness of approximately 2.29 Å. In order to obtain better surface morphology, then Sb/Ga flux should be optimized. We can see that there are many V group vacancies when the Sb/Ga BEP flux ratio is small, as shown in Fig. S5 (Sb/Ga = 3, 4, and 5). When the Sb/Ga BEP flux ratio is larger than 8, many three-dimensional network structures are produced on the surface, as shown in Figs. S5 (Sb/Ga = 10 and 11) and S3 (Sb/Ga = 9 and 10). This is caused by too many Sb atoms adsorbed on the surface, and excess Sb atoms lead to the growth model transforming into an island growth model. Too much or too little Sb atom flux causes the surface to be rough. When the Sb/Ga BEP flux ratio is 8, the smallest RMS surface roughness was obtained, as shown in Figs. 2(f), S4 and S5. The AFM images show an RMS surface roughness of approximately 1.63 Å and clear atomic steps over an area of 10×10 μm^2 and 5×5 μm^2 as shown in Fig. 2(f).

The period thickness of the 12.5 ML/8 ML InAs/GaSb superlattice epitaxial layer was extracted from HRXRD. The HRXRD measurements agree well with the simulation results, as shown in Fig. 3. The measured period of this material is approximately 61.44 Å (theoretical period thickness is 62.22 Å), as shown in Fig. 3, and the high-resolution x-ray diffraction exhibits high-order satellite peaks, which indicate that the epitaxial material possesses high quality.

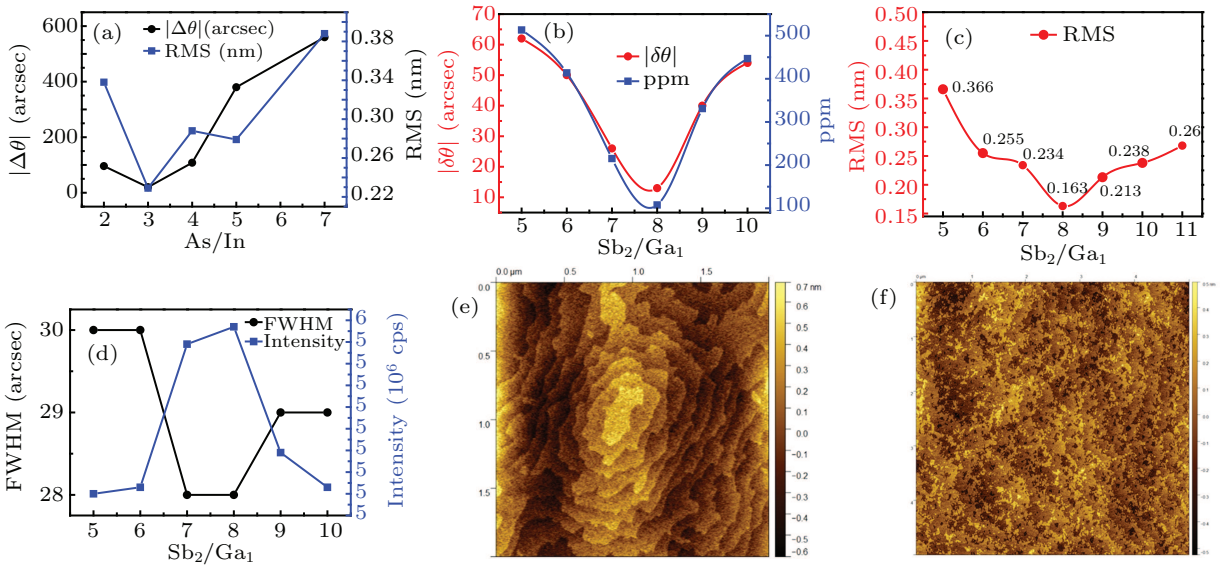


Fig. 2. The material quality of the samples. (a) The mismatch (arcsec) and RMS at different As/In BEP fluxes. (b) The mismatch (arcsec/ppm) at different As/In Sb/Ga BEP fluxes. (c) Surface roughness at different Sb/Ga BEP flux. (d) The FWHM and intensity of the zero-order peak at different Sb/Ga BEP fluxes. (e) The AFM image of As/In$_{\mathrm{BEP=3}}$ (2×2 μm^2). (f) The AFM image of Sb/Ga$_{\mathrm{BEP=8}}$ (5×5 μm^2).

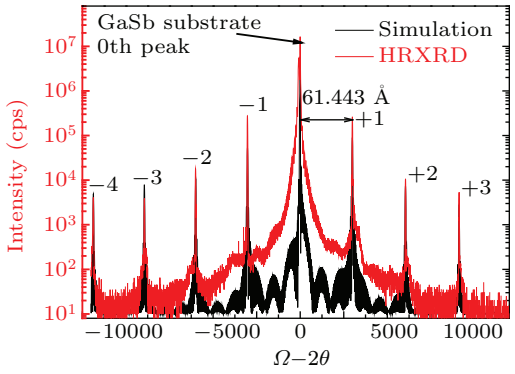


Fig. 3. High-resolution x-ray diffraction and simulation results.

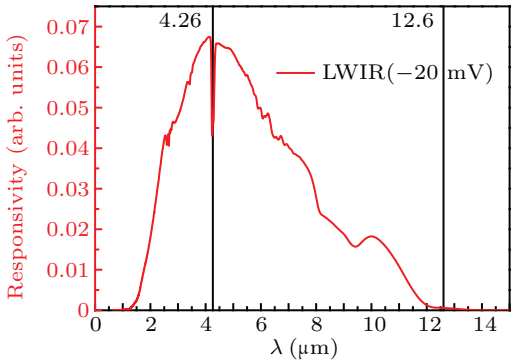


Fig. 4. The relative spectral response of LWIR detector.

Finally, an FTIR spectrometer was used to measure the relative spectral response of the LWIR detector at 77 K. The optical performance of the devices is shown in Fig. 4. The device exhibits a 100% cut-off wavelength of 12.6 μm under a 20 mV applied bias. The peak response wavelength is approximately 4 μm, in addition, there is a strong CO_2 absorption peak at 4.26 μm.

4. Conclusion

In summary, we have obtained high material quality InAs/GaSb type-II superlattice material for long-wavelength infrared range by using optimal V/III beam-equivalent pressure ratio, which is 8 and 3 with MEE method controlled InSb-like interface, and the experimental results indicate that we succeed in growing strain balanced and high quality InAs/GaSb superlattices on the GaSb substrate. In the following steps, we will improve the device performance of the LWIR detectors. High-quality epitaxial materials have laid a solid foundation for designing and manufacturing high-performance infrared photodetectors.

Acknowledgements

Project supported by the National Key Technology R&D Program of China (Grant Nos. 2018YFA0209104, 2018YFA0209102, 2019YFA0705203, and 2019YFA070104), the National Natural Science Foundation of China (Grant Nos. 61790581, 61274013, and 62004189), and the Key Research Program of the Chinese Academy of Sciences (Grant No. XDPB22).

References

[1] Sai Halasz G A, Tsu R and Esaki L 1977 *Appl. Phys. Lett.* **30** 651
[2] Smith D L and Mailhiot C 1987 *J. Appl. Phys.* **62** 2545
[3] Tennant W E, Lee D, Zandian M, Piquette E and Carmody M 2008 *J. Electronic Mater.* **37** 1406
[4] Lee D, Carmody M, Piquette E, Dreiske P, Chen A, Yulius A, Edwall D, Bhargava S, Zandian M and Tennant W E 2016 *J. Electronic Mater.* **45** 4587
[5] Reine M B, Sood A K and Tredwell T J 1981 *Mercury Cadmium Telluride* (Amsterdam: Elsevier) pp. 201–311
[6] Kruse P W 1981 *Mercury Cadmium Telluride* (Amsterdam: Elsevier) pp. 1–20
[7] Chen X, Zhang W and Ye Z 2018 *Infrared Technology and Applications XLIV* p. 1
[8] Hirsch H E, Liang S C and White A G 1981 *Mercury Cadmium Telluride* (Amsterdam: Elsevier) pp. 21–45
[9] Micklethwaite W F H 1981 *Mercury Cadmium Telluride* (Amsterdam: Elsevier) pp. 47–119
[10] Krishnamurthy S B M A, Robinson H and Sher A 2006 *J. Electronic Mater.* **35** 1399
[11] Petersen P E 1981 *Mercury Cadmium Telluride* (Amsterdam: Elsevier) pp. 121–155
[12] Angeloscotty G, James B and Amanda G 2006 *J. Electronic Mater.* **35** 1403
[13] Rogalski A 2011 *Infrared Phys. Techn.* **54** 136
[14] Liao K S L Z F, Wang C, Li L, Zhou X H, Li N and Dai N 2016 *J. Infrared Millim. Waves* **35** 0037
[15] Hubert J M R, Nicholas R S, Francis P, Timothy D P, Marc L, Mario L, Ghislain B, Martin P, Danick A and Philippe L 1996 *Micromachined Devices and Components II* pp. 111–121
[16] Zhou J, Raihan Miah M A, Yu Y, Zhang A C, Zeng Z, Damle S, Niaz I A, Zhang Y and Lo Y H 2019 *Opt. Express* **27** 37056
[17] Andresen B F, Rogalski A, Fulop G F and Norton P R 2006 *Proc. SPIE* **6206** 620601
[18] Rogalski A, Martyniuk P and Kopytko M 2017 *Appl. Phys. Rev.* **4** 031304
[19] Rogalski A, Martyniuk P and Kopytko M 2019 *Prog. Quantum Electron.* **68** 100228
[20] Gautam N, Myers S, Barve A V, Klein B, Smith E P, Rhiger D R, Dawson L R and Krishna S 2012 *Appl. Phys. Lett.* **101** 021106
[21] Deng G, Yang W, Zhao P and Zhang Y 2020 *Appl. Phys. Lett.* **116** 031104
[22] Gunapala S D, Ting D and Rafol S, *et al.* 2021 *Infrared Technology and Applications XLVII* p. 117410
[23] Youngdale E R, Meyer J R, Hoffman C A, Bartoli F J, Grein C H, Young P M, Ehrenreich H, Miles R H and Chow D H 1994 *Appl. Phys. Lett.* **64** 3160
[24] Wei Y and Razeghi M 2004 *Phys. Rev. B* **69** 085316
[25] Chen X, Cao X, Zhang L, Zhang L and He Y 2016 *Opt. Quantum Electron.* **48** 0375
[26] Binhminh N, Guanxi C, Minhanh H and Razeghi M 2011 *IEEE J. Quantum Electron.* **47** 686
[27] Cui S N, Jiang D W, Sun J, Jia Q X, Li N, Zhang X, Li Y, Chang F R, Wang G W, Xu Y Q and Niu Z C 2020 *Chin. Phys. B* **29** 048502
[28] Hood A, Razeghi M, Aifer E H and Brown G J 2005 *Appl. Phys. Lett.* **87** 151113
[29] Sullivan G J, Ikhlassi A, Bergman J, DeWames R E, Waldrop J R, Grein C, Flatteé M, Mahalingam K, Yang H, Zhong M and Weimer M 2005 *J. Vacuum Sci. Techn.* **23** 1144
[30] Jiang D, Xiang W, Guo F, Hao H, Han X, Li X, Wang G, Xu Y, Yu Q and Niu Z 2016 *Appl. Phys. Lett.* **108** 121110
[31] Chow D H, Miles R H and Hunter A T 1992 *J. Vacuum Sci. Techn. B* **10** 888
[32] Liu Y F, Zhang C J, Wang X B, Wu J and Huang L 2021 *Infrared Phys. Techn.* **113** 103573
[33] Nguyen B M, Hoffman D, Delaunay P Y and Razeghi M 2007 *Appl. Phys. Lett.* **91** 163511
[34] Klipstein P C, Benny Y, Gliksman S, Glozman A, Hojman E, Klin O, Langof L, Lukomsky I, Marderfeld I, Nitzani M, Snapi N and Weiss E 2019 *Infrared Phys. Techn.* **96** 155
[35] Bracker A S, Yang M J, Bennett B R, Culbertson J C and Moore W J 2000 *J. Crystal Growth* **220** 384